PROCEEDINGS OF SPIE

SPIEDigitalLibrary.org/conference-proceedings-of-spie

Modeling the vortex center glow in the ELT/METIS vortex coronagraph

Muskan Shinde, Christian Delacroix, Gilles Orban de Xivry, Olivier Absil, Roy van Boekel

Muskan Shinde, Christian Delacroix, Gilles Orban de Xivry, Olivier Absil, Roy van Boekel, "Modeling the vortex center glow in the ELT/METIS vortex coronagraph," Proc. SPIE 12187, Modeling, Systems Engineering, and Project Management for Astronomy X, 121870E (25 August 2022); doi: 10.1117/12.2629855

SPIE.

Event: SPIE Astronomical Telescopes + Instrumentation, 2022, Montréal, Québec, Canada

Modeling the vortex center glow in the ELT/METIS vortex coronagraph

Muskan Shinde[a*], Christian Delacroix[b], Gilles Orban de Xivry[b], Olivier Absil[b], Roy van Boekel[c]
[a] Indian Institute of Science Education and Research (IISER) Pune, Dr. Homi Bhabha Rd, Pashan, Pune 411008, India
[b] Space sciences, Technologies, and Astrophysics Research (STAR) Institute, Université de Liège, Allée du Six Août 19C, 4000 Liège, Belgium
[c] Max-Planck-Institut für Astronomie (MPIA), Königstuhl 17, 69117 Heidelberg, Germany

ABSTRACT

The Mid-infrared ELT Imager and Spectrograph (METIS) is among the first three scientific instruments commissioned at the ELT. It will implement vortex coronagraphy to achieve high-contrast imaging (HCI) at small angular separations from bright, nearby stars. An important unresolved problem with vortex coronagraphy is the vortex center glow (VCG) effect, where the thermal emission from the warm environment around the entrance pupil is partially diffracted into the image of the pupil by the vortex phase mask (VPM), which shows up as a diffuse bright spot in the center of the image. This effect has proven to be a significant nuisance in previous mid-infrared observations. Here, we use physical optics propagation to model the VCG for the first time and evaluate its strength with respect to the background flux in standard non-coronagraphic imaging in the context of ELT/METIS. Through our end-to-end simulations we find that the VCG peaks at about 70% of the standard background flux at an angular separation of 1 λ/D from the star and reduces to about 20% at 5 λ/D from the star. We apply the same method to model the VCG for the VLT/VISIR configuration, and show our model to be in agreement with the actual VCG measured in VISIR data, where the peak of the VCG is about twice as bright as the thermal background. In case the VCG turns out to be larger than anticipated in METIS, we propose two methods to mitigate it: (i) adding pupil stops in the pupil plane upstream to the VPM to block all of the thermal emission, and (ii) adding undersized Lyot stops in the image plane to block part of the diffracted light.

Keywords: extremely large telescope, mid-infrared instrumentation, high-contrast imaging, vortex coronagraph, end-to-end simulations, ELT/METIS

1. INTRODUCTION

The field of coronagraphic imaging has made great advancements in the last two decades. Several new elegant coronagraphic concepts have been implemented to deal with starlight suppression in dedicated high-contrast imaging (HCI) instruments equipped with extreme adaptive optics systems, for example VLT/SPHERE[1], Gemini/GPI[2], and Subaru/SCExAO[3] (see review by Ruane et al. 2018[4] and Goździewski et al. 2010[5]). These coronagraphs can be classified into four broad categories based on the location of the coronagraphic mask (pupil plane or focal plane) and the way it modulates the stellar PSF (amplitude modulation or phase modulation).

The vortex coronagraph[6,7], consisting of a focal-plane phase mask, is one of the most efficient coronagraphs to observe very faint sources close to bright stars, as it offers a small inner working angle along with high throughput. It consists of a vortex phase mask (VPM) that introduces a phase shift of the form $e^{il\theta}$, where l is the topological charge and θ is the azimuthal coordinate, onto the stellar light in a focal plane, while leaving the off-axis planetary light (mostly) unaffected. This phase ramp is such that it leads to total destructive interference of light for a circular pupil and creates a dark core, an optical vortex[8]. This optical vortex propagates unaltered through the instrument[9] and provides a completely clear 360° discovery space. There are two kinds of VPMs: scalar and vector. Scalar VPMs are based on a structural phase ramp, which is highly dependent on the wavelength of the incoming light[7,10]. On other hand, vector VPMs are based on a

*E-mail: muskan.shinde@students.iiserpune.ac.in

Modeling, Systems Engineering, and Project Management for Astronomy X, edited by George Z. Angeli, Philippe Dierickx, Proc. of SPIE Vol. 12187, 121870E
© 2022 SPIE · 0277-786X · doi: 10.1117/12.2629855

"geometrical" phase, and can overcome this limitation. The vector VPM provides an achromatic "geometrical" phase shift which is obtained by manipulating the transverse polarization state of the light with space-variant birefringent elements[11,12]. The Annular Groove Phase Mask (AGPM)[6] is a charge-2 vector vortex coronagraph made up of a concentric, circular, space-variant, sub-wavelength grating etched onto a diamond substrate[13]. It has been installed at various HCI instruments, including VLT/NACO[14], VLT/VISIR[15], LBT/LMIRCam[16], and Keck/NIRC2[17], and has achieved remarkable broadband performance in the mid-infrared[18]. Its exquisite performance makes AGPM a good candidate for installation in future high-contrast mid-infrared imagers, such as ELT/METS[19].

However, there is an unresolved problem associated with vortex coronagraphs. During optical propagation through a vortex coronagraph, the thermal emission from the warm telescope environment around the entrance pupil is partially diffracted into the image of the pupil by the VPM, thereby creating a diffuse bright spot around the optical axis in the downstream image plane[18]. This effect is referred to as vortex center glow (VCG), and has proven to be a significant nuisance in previous mid-infrared observations with the vortex coronagraph[20]. In this work, we model the VCG in the vortex coronagraph of the ELT/METIS instrument. In Section 2, we provide an overview of the ELT/METIS instrument and describe its optical design. In Section 3, we describe thermal background emission coming from different parts of the telescope. We present the framework of our simulations in Section 4, and the results are shown in Section 5. To validate our simulations, we model the VCG in the VLT/VISIR instrument in Section 6. Finally, we summarize our conclusions in Section 7.

2. THE ELT/METIS INSTRUMENT

The Mid-infrared ELT Imager and Spectrograph (METIS)[21] is among the first three scientific instruments to be commissioned at the Extremely Large Telescope (ELT). One of its main science goals is the detection and characterization of exoplanets. METIS will provide HCI over the thermal-infrared wavelength range of 3-13 μm, covering L (2.9-4.1 μm), M (3.9-5.3 μm), and N (8.0-13.5 μm) bands, using advanced coronagraphic techniques like vortex coronagraphs and apodizing phase plates. Moreover, it will offer high-resolution (R ~ 100,000) integral field spectroscopy from 2.9 to 5.3 μm. Combining high-resolution spectroscopy with HCI, METIS will allow the detection and spectroscopic characterization of a variety of exoplanets, from transiting and non-transiting hot-Jupiters to Neptune-like objects and potentially even super-Earths[22].

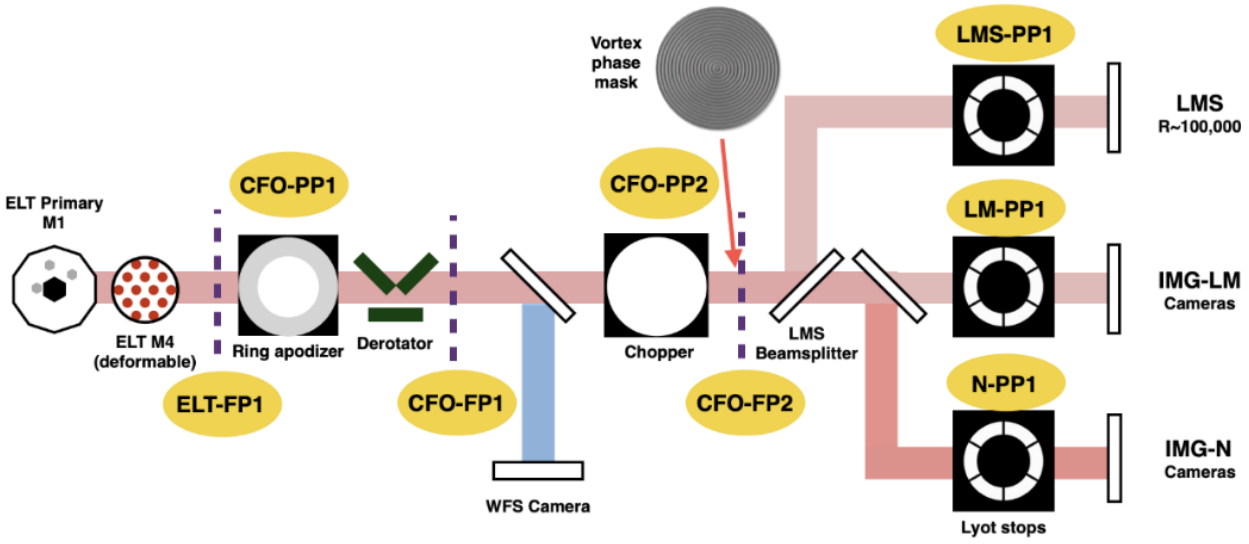

Figure 1: A schematic optical layout of METIS showing relevant optical components for (apodized) vortex coronagraphy.

2.1 METIS optical design

The METIS cryostat consists of four main subsystems: the common fore-optics (CFO) subsystem, which provides the optomechanical interface for various subsystems and performs various important functionalities like atmospheric

dispersion compensation, derotation, pupil stabilization, chopping, and coronagraphy; the single-conjugated adaptive optics (SCAO) subsystem, which implements an infrared pyramid wavefront sensor (PyWFS) and controls the shape of the ELT-M4 deformable mirror; the IMG subsystem, which consists of a pair of diffraction-limited imaging cameras operating at LM-band and N-band (referred to as IMG-LM and IMG-N, respectively); and the LMS subsystem, which consists of an integral-field high-resolution spectrograph.[23,24]

Different optical components for HCI will be installed in the various pupil and focal planes located in various METIS subsystems. In the CFO subsystem, the CFO-PP1 pupil plane and the CFO-FP2 focal plane will host wheel mechanisms that can insert coronagraphic components into the beam. So will the IMG-LM-PP1 and IMG-N-PP1 pupil planes (collectively referred to as IMG-PP1) located inside the IMG subsystem and the LMS-PP1 pupil plane inside the LMS subsystem.[24] A schematic layout showing the relevant optical components for (apodized) vortex coronagraphy is given in Figure 1.

2.2 METIS Vortex Coronagraph

The METIS vortex coronagraph consists of an AGPM placed at the CFO-FP2 focal plane[25]. The AGPM is made up of a concentric, circular, space-variant, sub-wavelength grating with rectangular grooves of depth h equally separated by the period Λ, which creates a charge-2 optical vortex[6]. A Lyot stop is placed at the subsequent IMG-PP1 pupil plane to block the starlight diffracted outside the pupil image by the AGPM. This design for the vortex coronagraph is called the classical vortex coronagraph (CVC). The optical layout of the METIS CVC is shown in Figure 2. The CVC provides a perfect on-axis stellar light cancellation for a circular, unobstructed pupil. However, in the presence of central obscuration, this property breaks down and leads to stellar leakage. Another vortex coronagraph design called the ring-apodized vortex coronagraph (RAVC) is implemented to compensate for the effect of the presence of a central obscuration. In this design, a third optical element called the ring apodizer is placed at the pupil plane upstream of the AGPM. This ring apodizer is designed such that it completely removes stellar light from a particular region in the Lyot stop plane for a purely annular pupil.

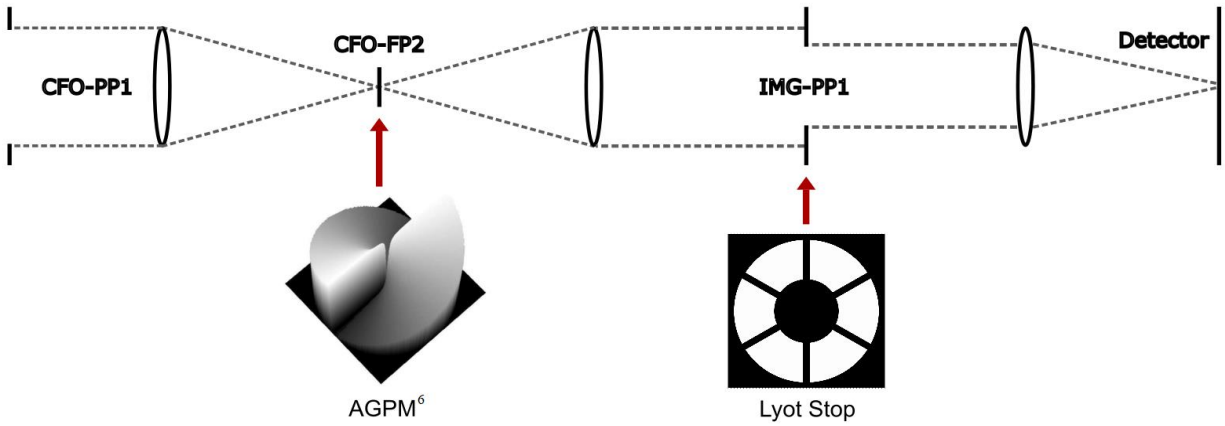

Figure 2: A schematic optical layout of the METIS CVC.

3. THERMAL BACKGROUND CONTRIBUTORS

The background emission comes from different parts of the telescope, including the environment around the entrance pupil, the spiders, the telescope glass, and the self-emission from the entrance window. In the METIS vortex coronagraph, the thermal background emission coming from the warm telescope environment and the spiders is partially diffracted into the image of the pupil by the AGPM, thereby creating a diffuse bright spot around the optical axis in the downstream image plane and leading to the VCG effect. To cut down a part of this background emission, a cold stop is placed in a pupil plane upstream of the AGPM.

3.1 ELT- M1 pupil geometry

The ELT primary mirror (ELT-M1) is a 39-m-diameter mirror made up of 798 1.45-m-wide hexagonal segments with 4-mm gaps between them. It is divided into six sectors by six 54-cm-wide spider arms, which are the shadows of the secondary support structure. In this study, for the sake of simplicity, we approximate the ELT pupil as an annular pupil with spider shadows, using the average outer and inner diameters. We checked that a more detailed model (using the actual pupil edges) does not significantly change the conclusions of this study. The geometry of the ELT-M1 pupil is shown in Figure 3. The red circles correspond to the average circular diameters of the ELT-M1 mirror, i.e., the equivalent inner and outer diameters providing the same collecting area as the ELT-M1 mirror. The ELT-M1 pupil dimensions are listed in Table 1.

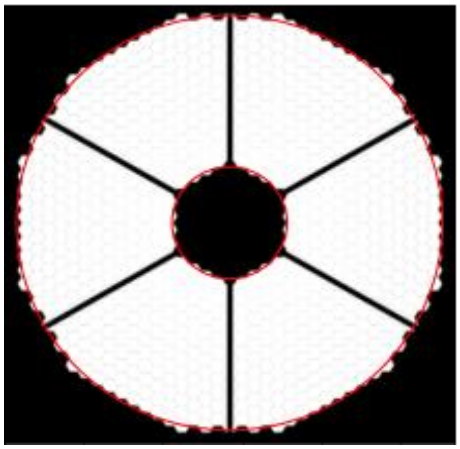

Figure 3: The ELT-M1 pupil geometry, with inner and outer red circles corresponding to the inner and outer average diameters, respectively.

Table 1: The ELT-M1 pupil dimensions.

notation	comment	diameter [m]
$d_{M1;in}$	minimum M1 diameter	9.418
$d_{Av;in}$	inner average diameter	10.196
$d_{Av;out}$	outer average diameter	37.812
$d_{M1;out}$	maximum M1 diameter	39.146

3.2 Background regions

The warm telescope environment and the ELT spiders are the main contributors to the vortex center glow. They are classified into the following regions:

1. the region beyond the ELT pupil's outer edge, i.e., the area outside the outer average diameter;
2. the region inside the central obscuration, i.e., the area inside the inner average diameter;
3. the region defined by the ELT spiders.

The region beyond the ELT pupil's outer edge and the region inside the central obscuration have the same background intensity and are collectively referred to as the environment. The expected background intensities, in the ELT-M1 plane, from the environment and the spiders, along with background intensities from other standard background contributors, consisting of the sky background, the telescope glass background, and the self-emission from the entrance window, are listed in Table 2. A part of the background from the spiders and the environment is stopped at IMG-PP1 or LMS-PP1 with a proper, undersized cold stop (which also serves as a Lyot stop in the case of vortex coronagraph). The expected background intensities, in the detector plane, from other standard background contributors are listed in Table 3.

Table 2: Background intensities in the pupil (IP), in the ELT-M1 plane, as seen from the CFO-FP2 plane.[26]

filter	wavelength range	baseline wavelength	IP_{spid}	IP_{env}	IP_{sky}	IP_{glass}	IP_{win}
			[10^3 photons/s/pix/m^2]				
L'	3.50 - 4.10 µm	3.82 µm	1.0010	1.213	0.0703	0.2125	0.0284
N2	10.10 - 12.40 µm	11.25 µm	494.3	594.8	14.97	100.6	18.61

Table 3: Background intensities (BG) from the standard background contributors, in the detector plane.[26]

filter	BG_{sky}	BG_{glass}	BG_{win}	total
	[10^6 photons/s/pix]			
L'	0.06475	0.2040	0.02723	0.30747
N2	13.80	96.54	17.87	128.21

3.3 CFO-PP1 cold stop

A cold stop consisting of a circular mask that forms the outer edge and a chopper mushroom that forms the inner edge, is placed upstream of the AGPM, in the CFO-PP1 pupil plane, to cut down part of the thermal emission from the background environment. However, there are some constraints on the size of the cold stop based on the stability of the ELT pupil. Since the CFO-PP1 is located upstream of the derotator and the pupil stabilization mirror, the image of the ELT pupil will drift with respect to the position of CFO-PP1 during observations. To keep the full ELT pupil image unvignetted at all times, the cold stop needs to be oversized. As a result, it does not completely block the background emission. The cold stop dimensions are given in Table 4.

Table 4: The cold stop dimensions, as seen from the ELT-M1 pupil.

notation	comment	diameter [m]
$d_{CS;in}$	cold stop inner edge diameter	7.363
$d_{CS;out}$	cold stop outer edge diameter	40.944

4. SIMULATIONS

The thermal background emission coming from different parts of the telescope is incoherent and cannot be simulated in a single optical propagation. To model this incoherent emission, we take small test apertures of radius a as representative of independent point sources in the telescope pupil. We propagate these test apertures, one by one, through the METIS CVC, using the HCI end-to-end performance simulator (HEEPS[27]), to infer their associated fluxes on the detector. Then we sum the contributions of all these small apertures to get the total flux on the detector, which is basically the VCG.

4.1 Test apertures

We take small circular apertures (with ones inside and zeros outside) of diameter $2a$ = 20 cm, which corresponds to about 1 pixel in a 285-pixel pupil grid. The flux of a test aperture is scaled by its area to get the flux in units of [photons/s/m^2] in the pupil plane. Different regions are sampled using these test apertures as follows:

1. The region beyond the ELT pupil's outer edge: test apertures starting from the pupil's outer edge (defined by the outer average diameter) to the cold stop's outer edge, sampled at every 5-degree azimuth.
2. The region inside the central obscuration: test apertures starting from the pupil's inner edge (defined by inner average diameter) to the cold stop's inner edge, sampled at every 10-degree azimuth.
3. The region along the ELT spiders: test apertures along both edges of all the six spiders, starting from the pupil's inner edge to the pupil's outer edge.

Figure 4 shows the way the ELT pupil is sampled using the test apertures.

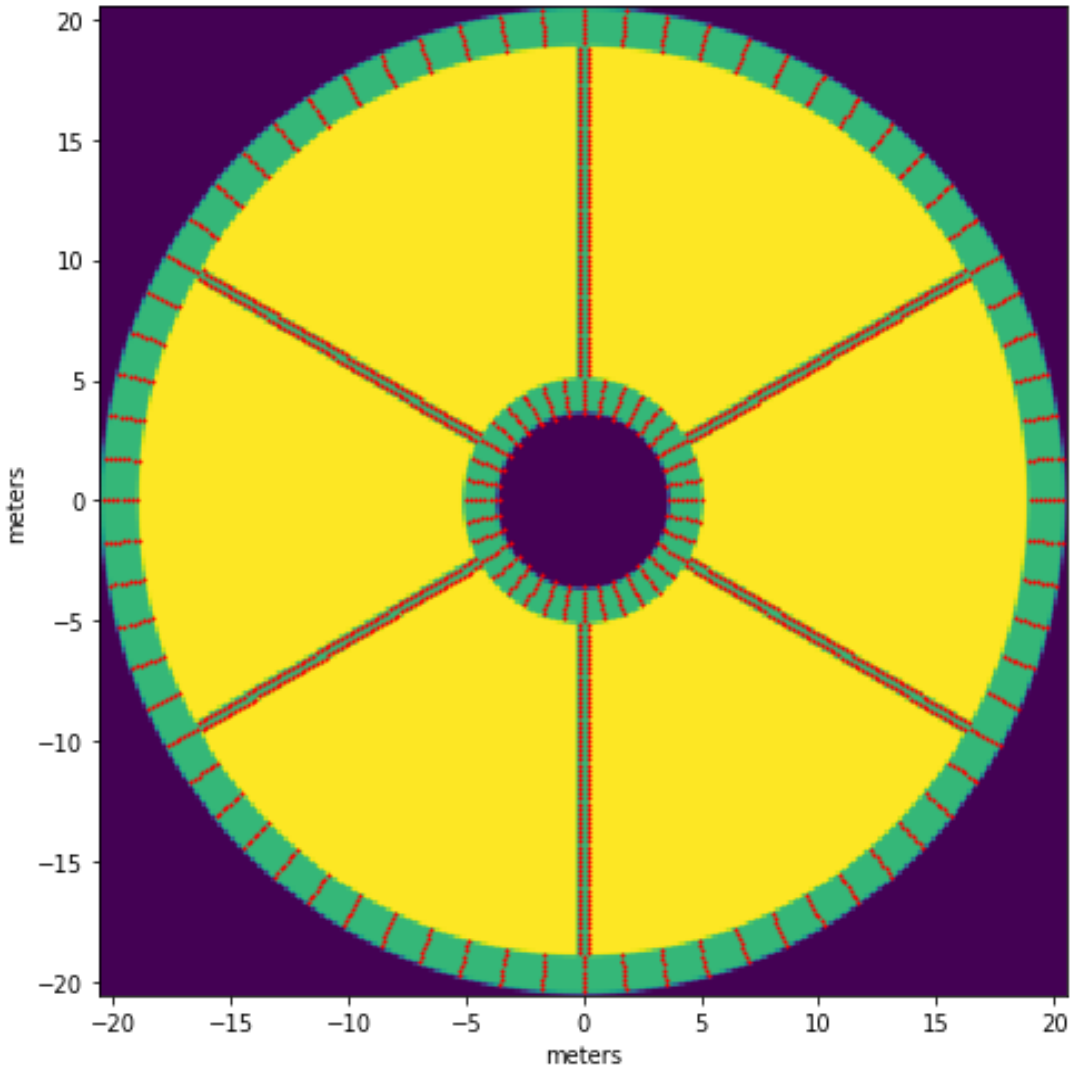

Figure 4: Test apertures (red dots) sampling the environment of our circularized version of the ELT-M1 pupil. The yellow part corresponds to the ELT-M1 average diameters, while the green regions represent the part of the telescope environment that makes it through to the oversized cold stop in CFO-PP1.

4.2 Focal-plane flux rescaling

For a single input aperture in the pupil plane, we get, in CFO-FP2, an Airy-like intensity pattern instead of a fully uniform background because the test apertures have a finite size (instead of being ideal point sources). The size of the Airy core is larger than the active zone of the vortex coronagraph, therefore the vortex sees a uniform illumination, so our approximation of taking small finite-sized test apertures is good enough. At CFO-FP2, we rescale the flux of the aperture to its actual flux level. Since the background flux levels per surface area (in photons/s/pix/m^2) predicted in van Boekel 2021[26] are given per pixel, we rescale the flux of the aperture pixel by pixel. To do this, we first normalize the intensity of the pixels by dividing them with the intensity of the pixel that has maximum intensity. Then we multiply them by their actual background intensity levels, i.e., by IP_{spid} for the spiders and by IP_{env} for the environment (see Table 2). After rescaling the flux, we apply the VPM, followed by an undersized Lyot stop in the IMG-PP1 pupil plane. The intensity distribution in the Lyot plane is shown in Figure 5 (left).

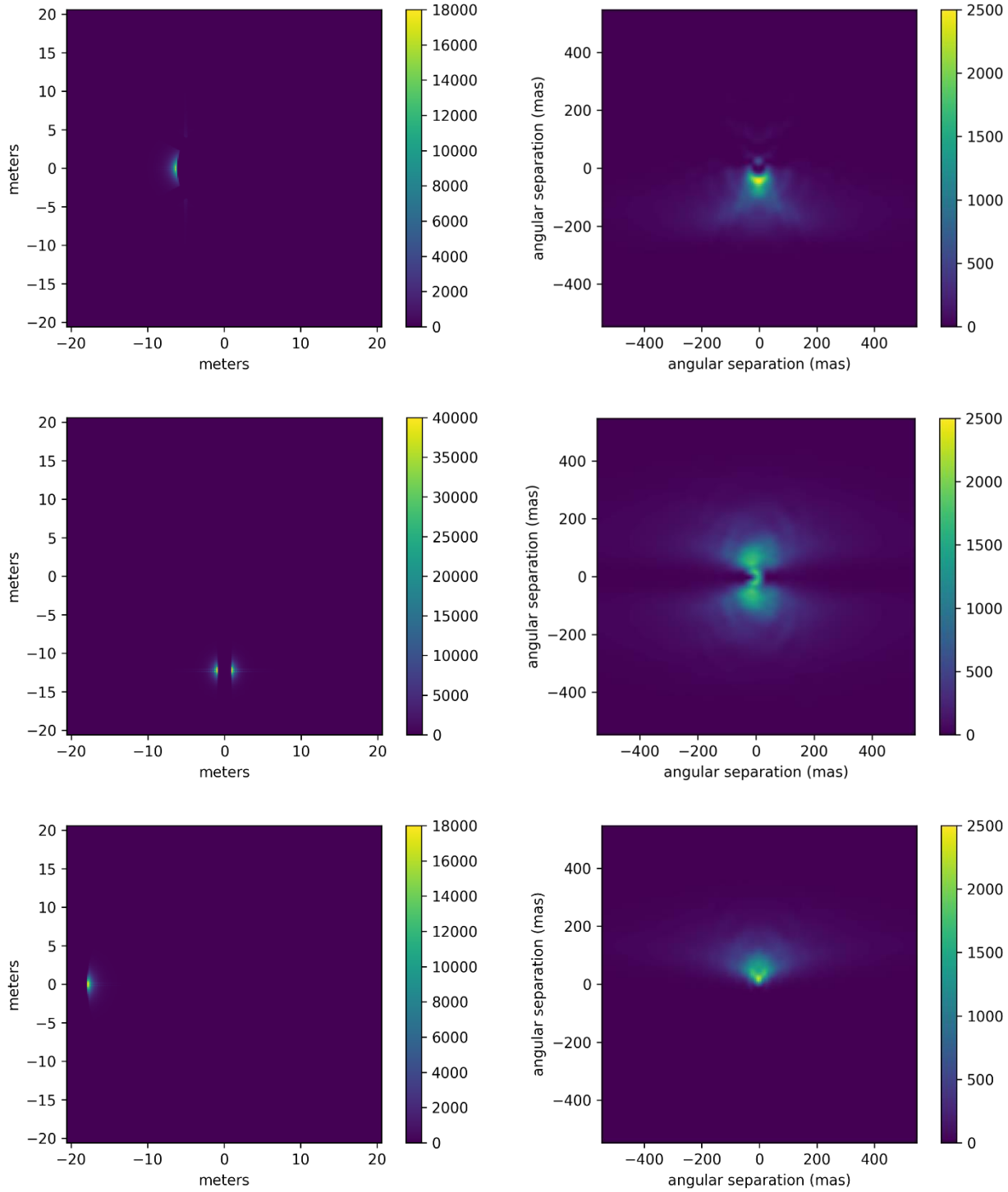

Figure 5: Intensity distribution in the Lyot plane (left) and the detector plane (right). Top: for a test aperture at the pupil's inner edge. Middle: for a test aperture in midway along a spider. Bottom: for a test aperture at the pupil's outer edge. The units of the intensity scales are [photons/s/pix/m^2].

4.3 Summing flux on detector

Finally, we get the net flux per surface area from each test aperture on the detector. The intensity distribution in the detector plane is shown in Figure 5 (right). To go from these individual test aperture fluxes to the net flux from a region, we scale the flux of the test apertures according to the surface area they sample and sum their contribution, which is done as follows:

1. For the environment:
   The net intensity for a circular annulus at a radial distance *r* is calculated by summing the intensities of all the test apertures taken at that particular radial distance, dividing by the number of test apertures, and multiplying by the area of the annulus (see Figure 6 (a)):

$$A_{annulus} = \pi(r+a)^2 - \pi(r-a)^2 = 4\pi ra \tag{1}$$

$$I_{annulus;r} = \sum_{i=1}^{n} I_{aperture;i} * \frac{A_{annulus}}{n} \tag{2}$$

   where *a* is the radius of a test aperture, and *n* is the total number of test apertures taken at the radial distance *r*. The total intensity of a region is calculated by summing the intensities of all the annuli in that region.

$$I_{region} = \sum_{r=r_{int}}^{r_{ext}} I_{annulus;r} \tag{3}$$

   where r_{int} and r_{ext} are the internal and external radii of the region, respectively.

2. For the spiders:
   The net intensity for a rectangular sub-part of a spider, at a radial distance *r*, is calculated by summing the intensities of both test apertures taken at that particular radial distance, diving by the number of test apertures (which is 2 in this case) and multiplying by the area of the rectangle (see Figure 6 (b)):

$$A_{rect} = 2a * w \tag{4}$$

$$I_{rect;r} = \frac{I_{aperture;right} + I_{aperture;left}}{2} * A_{rect} \tag{5}$$

   where *w* is the width of the spider. The total intensity of a spider is calculated by summing the intensities of all the rectangular sub-parts:

$$I_{spider} = \sum_{r=r_{int}}^{r_{ext}} I_{rect;r} \tag{6}$$

   where r_{int} and r_{ext} are the start and end radii of the spider, respectively.

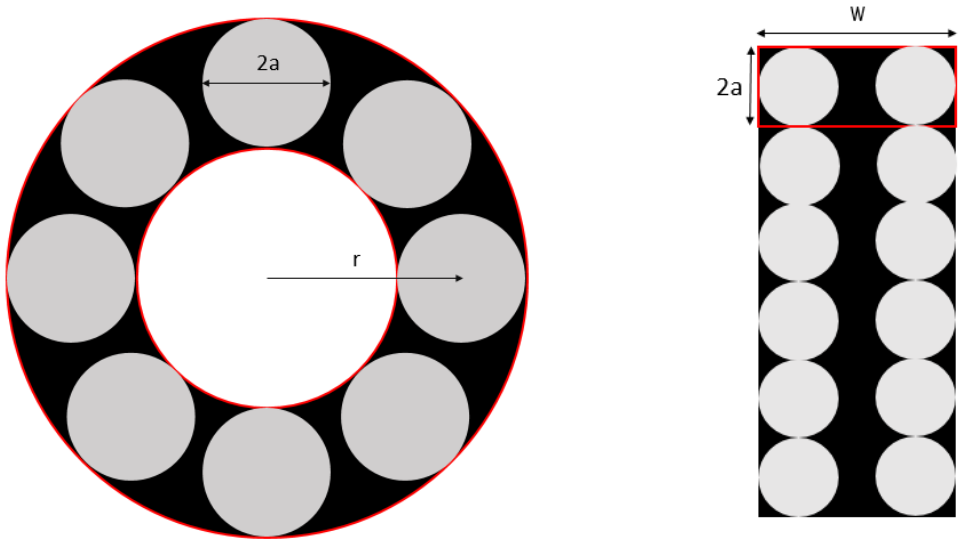

Figure 6: (a) Left: an annulus at a radial distance *r* from the center. (b) Right: a spider with a rectangular sub-part marked in red. Here, *a* denotes the radius of a circular test aperture and *w* denotes the width of the spider.

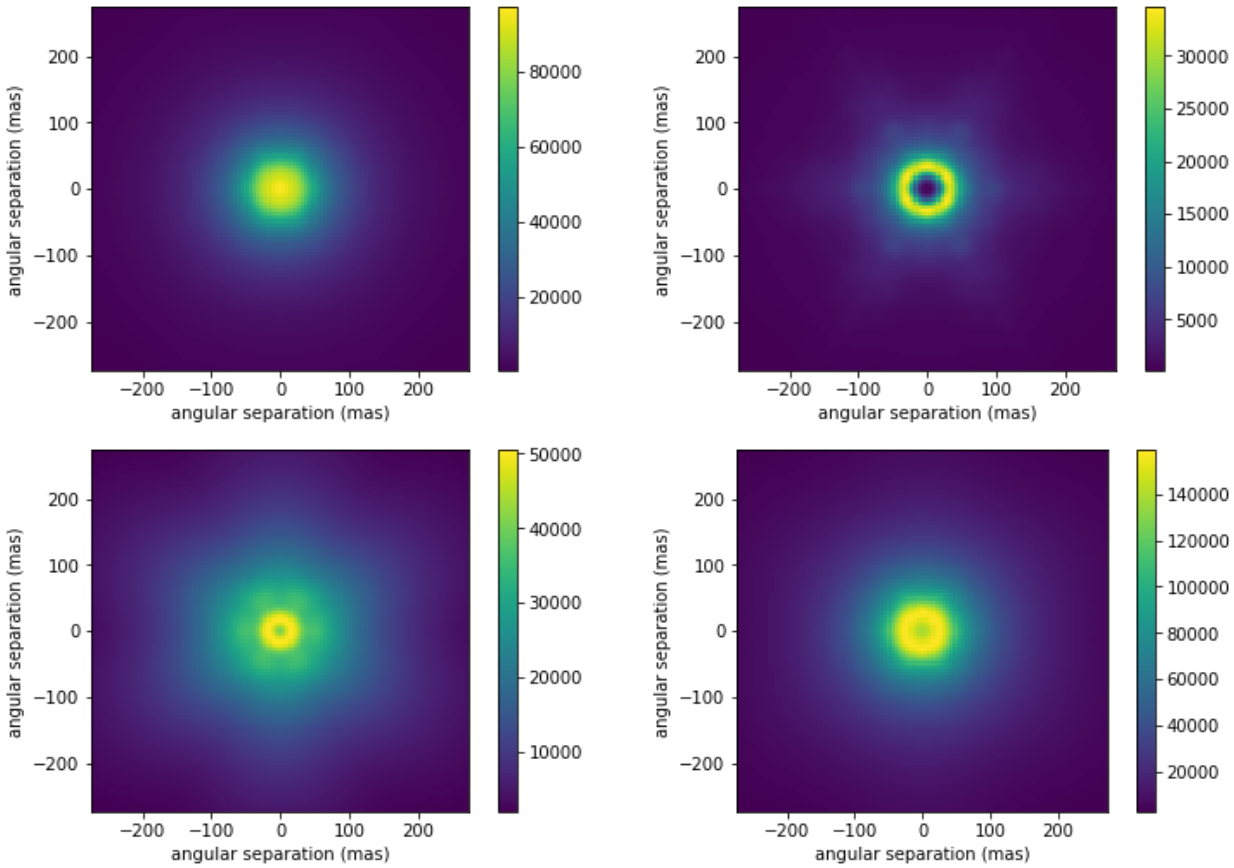

Figure 7: VCG contribution from different regions: (a) top-left: from beyond the ELT pupil's outer edge. (b) top-right: from inside the central obscuration. (c) bottom-left: from the ELT spiders. (d) bottom-right: the net VCG from all the regions. These images are obtained using the L' filter. The units of the intensity scales are [photons/s/pix].

5. RESULTS

5.1 Intensity of the VCG

The contribution of different background regions to the VCG is shown in Figure 7. Figure 7 (a) shows the VCG from the region beyond the ELT pupil's outer edge. We observe that the detector-plane intensity distribution we get from the thermal emission from points in this region looks like a (relatively compact) two-dimensional Gaussian. Figure 7 (b) shows the VCG from inside the central obscuration. The detector-plane intensity distribution we get from the emission from points in this region is doughnut-shaped. Because both the inner and outer contributions stem from an annulus of incoherent background, delimited by the ELT-M1 edge and the CFO-PP1 cold stop, our understanding is that the shape of the response in the focal plane is actually the same for both regions, but that the doughnut is not resolved in the case of the outer region. Figure 7 (c) shows the VCG we get from the region along the ELT spiders. Finally, the net VCG, summing up the contributions of all three regions, is shown in Figure 7 (d). The integrated VCG intensities are given in Table 5.

Figure 8 shows the radial profile of the VCG obtained from all three background regions. We see that for both the L' and N2 filters, the major contribution to the net VCG close to the optical axis comes from the region beyond the ELT pupil's outer edge, while the smallest contribution comes from the region inside the central obscuration. At an angular separation of 5 λ/D from the star, the net background flux from VCG is around 21% of the standard background flux for the L' filter, while for the N2 filter, it is 24%. Since the VCG flux is significantly less than the standard background flux at radial separations of interest, it will not significantly affect the HCI performance.

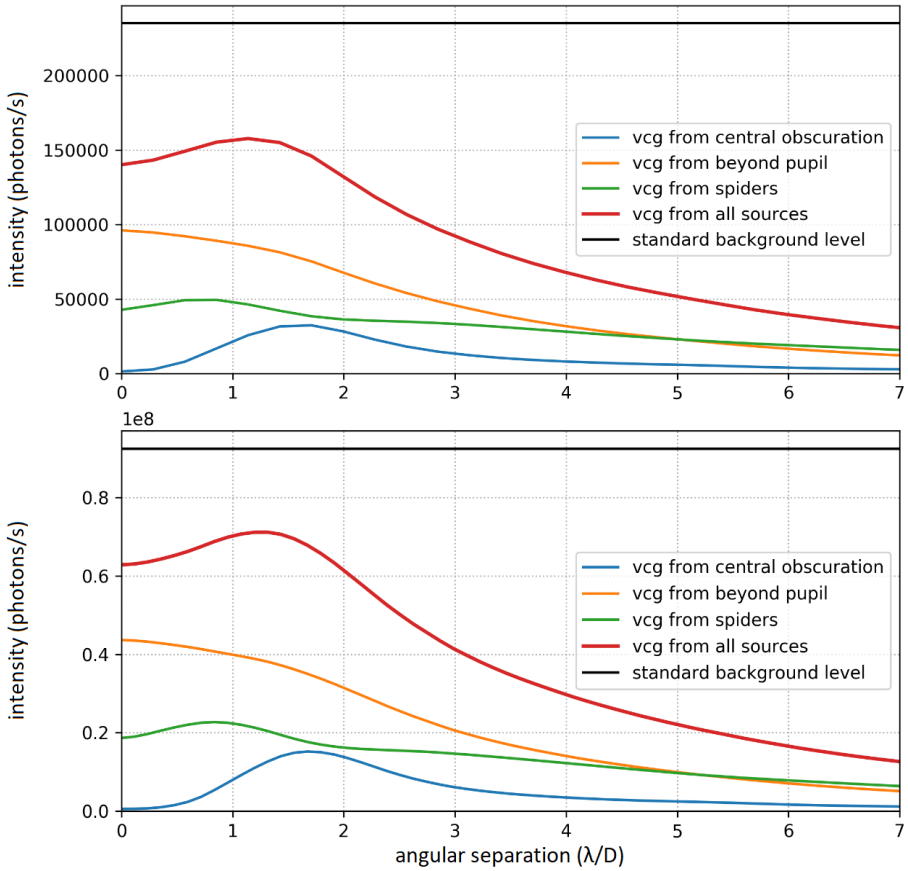

Figure 8: VCG radial profiles for: (a) top: L' filter (b) bottom: N2 filter. The blue curve is for the VCG from inside the central obscuration; the yellow curve is for the VCG from beyond the ELT pupil's outer edge; the green curve is for the VCG from the ELT spiders; the red curve is for the net VCG from all sources; and the black line denotes the background flux in standard non-coronagraphic imaging.

Table 5: Integrated VCG intensities from different background regions.

filter	VCG $_{\text{beyond pup edge}}$	VCG $_{\text{central obscuration}}$	VCG $_{\text{spiders}}$	VCG $_{\text{total}}$
	[10^9 photons/s]			
L’	0.112	0.0294	0.156	0.297
N2	231.79	61.78	260.28	553.85

5.2 Influence of the Lyot stop design

The above simulations were done taking the standard Lyot stop design, i.e., a Lyot stop with 2.91% outer edge undersize & inner edge oversize and a 3.71% spider oversize in the case of the L’ filter, whereas a Lyot stop with 3.56% outer edge undersize & inner edge oversize and a 3.83% spider oversize in the case of the N2 filter.

To determine the influence of the Lyot stop design on the VCG, we applied Lyot stops with various amounts of undersizing and calculated the net VCG flux. Figure 9 shows the variation of the net VCG flux with Lyot stop undersize. We observe that the VCG flux decreases both with the outer edge undersize & inner edge oversize, and with the spider oversize. However, the spider oversize leads to more VCG flux reduction as compared to the outer edge undersize & inner edge oversize. So, using more undersized Lyot stop designs, with the main focus on the spider oversize, will help in mitigating the VCG.

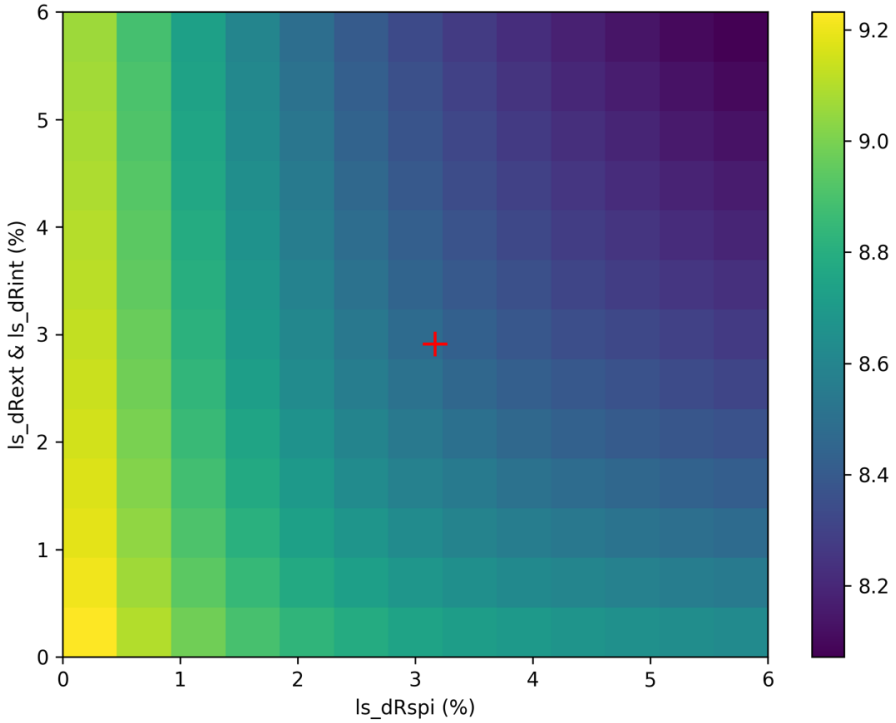

Figure 9: The net VCG at L’ band (log scale), mapped as a function of ls_dRext & ls_dRint (outer edge undersize and inner edge oversize, respectively) and ls_dRspi (spider oversize). The red cross marks the dimensions of the standard Lyot stop (ls_dRext & ls_dRint = 2.91% and ls_dRspi = 3.17%).

6. THE VLT/VISIR INSTRUMENT

The VLT Imager and Spectrometer for the mid-Infrared (VISIR) is an instrument that provides diffraction-limited imaging over the N (8-14 μm) and Q (17-28 μm) bands. In 2019, the New Earths in the Alpha Cen Region (NEAR) experiment was

launched to search for rocky exoplanets in the habitable zone around Alpha Centauri A and B with VISIR[28]. To enable HCI with VISIR, it was upgraded with a new vortex coronagraph consisting of an AGPM and was installed at the VLT unit telescope 4 to use the adaptive optics facility there.

To validate our simulations, we model the VCG for the VISIR instrument in the NEAR configuration, where no cold stop is present upstream of the AGPM.

6.1 VLT pupil geometry

The VLT primary mirror is an 8.2-m-diameter mirror with a 1.1-m-wide central obscuration. It is divided into four sectors by four 4-cm-wide spider arms, which are the shadows of the secondary support structure. The geometry of the VLT pupil is shown in Figure 10.

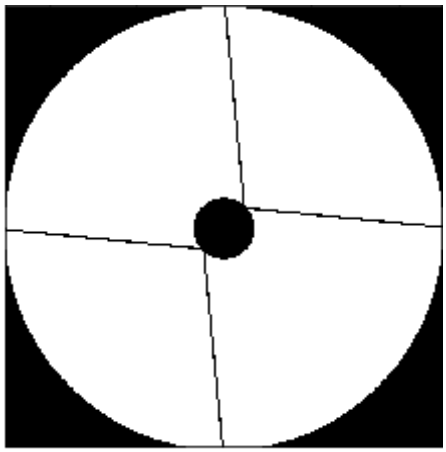

Figure 10: The VLT pupil geometry.

6.2 Background regions

The warm telescope environment and the spiders are the main contributors to the vortex center glow. They are classified into the following regions:

1. the region beyond the VLT pupil's outer edge;
2. the region inside the central obscuration;
3. the region along the spiders.

The background intensities from these regions in the VLT pupil plane and the background intensity from other standard background contributors in the detector plane, computed from L. Burtscher's Jupyter notebook†, are listed in Table 6.

Table 6: Background intensities in the pupil (IP) from the environment and spiders, and the net standard background level in the focal plane from all the standard background contributors, computed from L. Burtscher's Jupyter notebook†.

band	filter	baseline wavelength	IP_{spid}	IP_{env}	BG_{std}
			[10^6 photons/s/pix/m^2]		[10^7 photons/s/pix]
N band	B10.7	10.65 μm	3.69	4.44	2.15

† https://github.com/astroleo/visir_sensitivity/blob/master/VISIR%20sensitivity.ipynb

6.3 Intensity of the VCG

We model the background thermal emission and perform simulations in the same way as discussed in section 4. Figure 11 shows the VCG obtained from our simulations. Figure 11 (a) shows the VCG from the region beyond the pupil's outer edge, Figure 11 (b) shows the VCG from inside the central obscuration, and Figure 11 (c) shows the VCG we get from the region along the spiders. The net VCG is shown in Figure 11 (d). The VCG intensities are given in Table 7. The intensity distribution of the net VCG in VISIR, like in METIS, is doughnut-shaped. However, the doughnut is not as prominent in the case of VISIR.

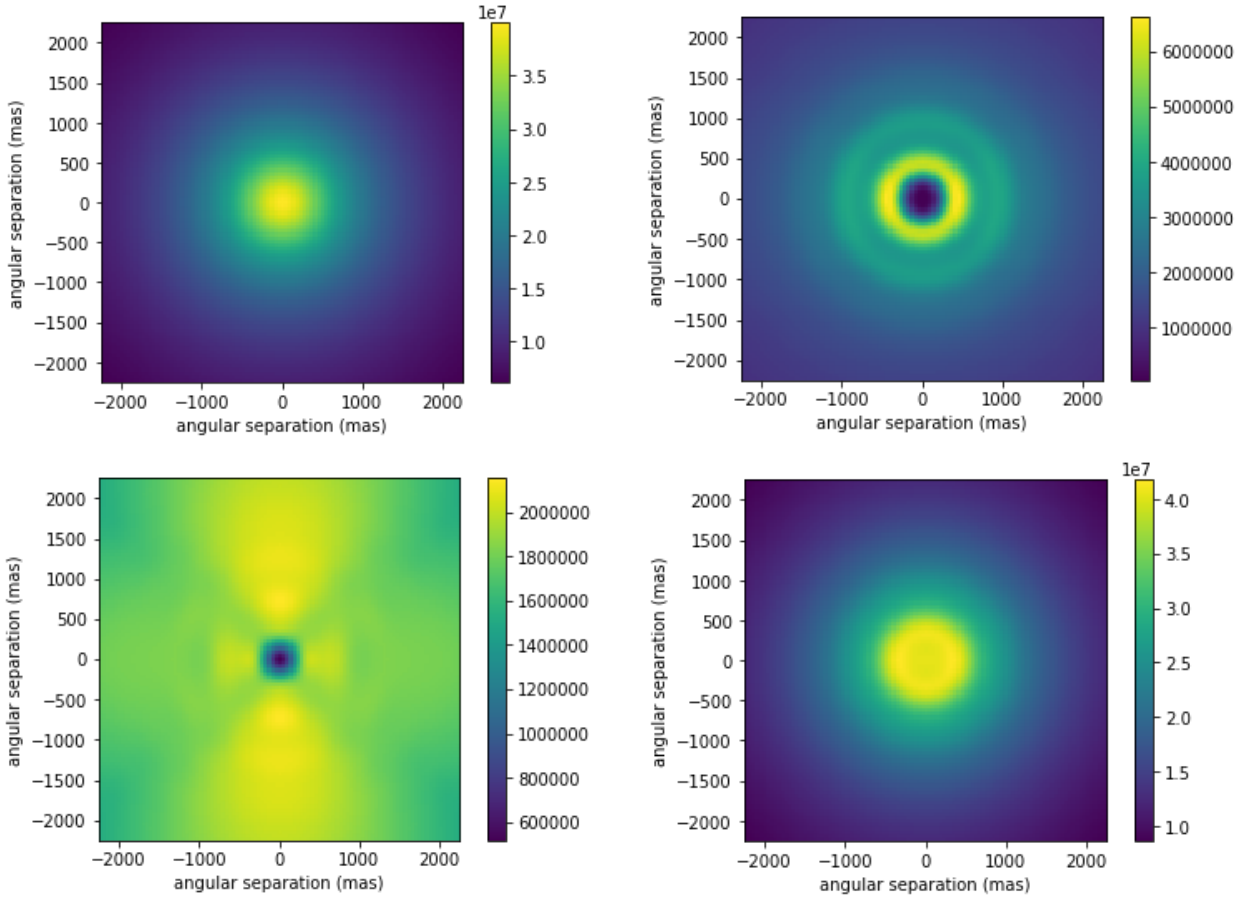

Figure 11: VCG contribution from different regions: (a) top-left: from beyond the pupil's outer edge. (b) top-right: from inside the central obscuration. (c) bottom-left: from the spiders. (d) bottom-right: the net VCG. The units of the intensity scales are [photons/s/pix].

Table 7: VISIR's VCG intensities from different background regions.

filter	VCG $_{\text{beyond pup edge}}$	VCG $_{\text{central obscuration}}$	VCG $_{\text{spiders}}$	VCG $_{\text{total}}$
	[10^{11} photons/s]			
B10.7	3.64	0.057	1.01	5.22

Figure 12 shows the radial profile of the VCG obtained. We see that the net VCG level is above the standard background flux level. The background flux from VCG is around 1.94 times the standard background flux, which is in accordance with the actual VCG observed in the case of VISIR as discussed in Maire et al. 2020[20], i.e., about twice as bright as the thermal background in non-coronagraphic imaging.

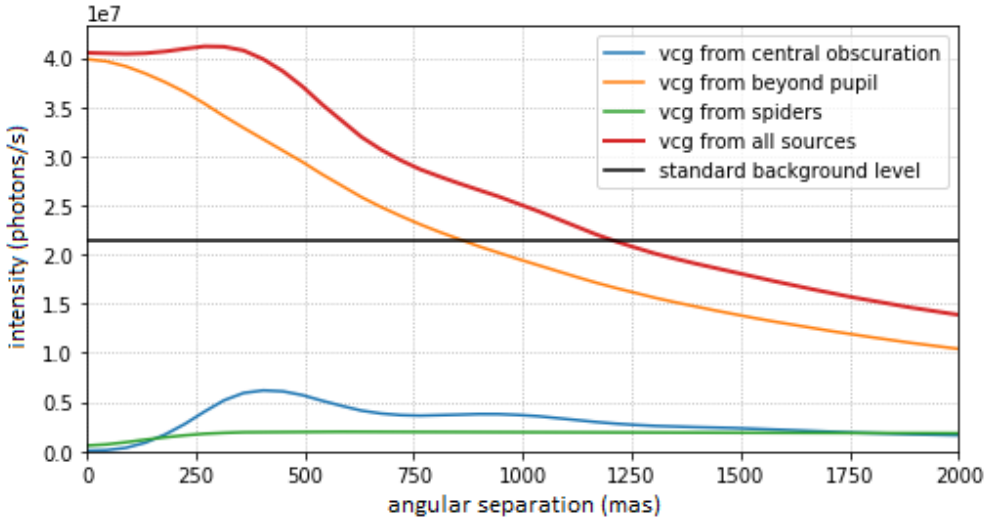

Figure 12: VCG radial profiles for VISIR. The blue curve is for the VCG from inside the central obscuration; the yellow curve is for the VCG from beyond the pupil's outer edge; the green curve is for the VCG from the spiders; the red curve is for the net VCG from all sources; and the black line denotes the background flux in standard non-coronagraphic imaging.

7. CONCLUSIONS

While the VCG brings some additional, unwanted background noise at the shortest angular separations, its contribution to the total background budget is not dominant. Furthermore, the VCG contribution to the background is constant in shape and brightness to the first order, thanks to the margin in the CFO-PP1 cold stop oversizing (which ensures that the ELT-M1 pupil is never vignetted), so that it will be automatically removed by background subtraction and/or ADI processing. The increase in required observing time associated with the VCG will be limited, especially when considering that the first few λ/D are usually dominated by speckle noise. For faint target stars, the benefits of using the vortex coronagraph will need to be weighed against the additional background noise, especially at the N band and for science cases that require very small inner working angles. Besides this additional background noise, we note that the VCG is also an asset for coronagraphic operations, as it provides a bright enough reference to accurately measure the position of the center of the vortex phase ramp onto the detector.

These simulations are sufficiently reassuring to continue with the METIS baseline design, which does not include any undersized cold stop upstream of the vortex coronagraphs. However, simulations are never perfect, and we cannot exclude that the assumptions used to model the ELT thermal environment are not sufficiently representative. This is the reason why we recommend adding a series of undersized cold stops in CFO-PP1, to be used as a backup in case the VCG turns out to be brighter than expected from our simulations. The use of these backup cold stops would then need to be traded against the significant loss in throughput they are associated with. Another possible way to mitigate the VCG would be to use more undersized Lyot stops. The relative benefits of these two mitigation plans (cold stops in CFO-PP1 or Lyot stops) would depend on the magnitude of the effect.

ACKNOWLEDGEMENTS

We thank L. Burtscher, our colleague at Leiden Observatory, for sharing his jupyter notebook that helped us evaluate the background flux levels in VLT/VISIR. We are grateful to all the METIS consortium teams, especially to the HCI team, for helpful conversations.

REFERENCES

[1] Beuzit, J.-L., Feldt, M., Dohlen, K., Mouillet, D., Puget, P., Wildi, F., Abe, L., Antichi, J., Baruffolo, A. and Baudoz, P., "SPHERE: a planet finder instrument for the VLT," Ground-based and airborne instrumentation for astronomy II **7014**, 476–487, SPIE (2008).

[2] Macintosh, B., Graham, J., Palmer, D., Doyon, R., Gavel, D., Larkin, J., Oppenheimer, B., Saddlemyer, L., Wallace, J. K. and Bauman, B., "The Gemini planet imager," Advances in Adaptive Optics II **6272**, 177–188, SPIE (2006).

[3] Lozi, J., Guyon, O., Jovanovic, N., Goebel, S., Pathak, P., Skaf, N., Sahoo, A., Norris, B., Martinache, F. and N'Diaye, M., "SCExAO, an instrument with a dual purpose: perform cutting-edge science and develop new technologies," Adaptive Optics Systems VI **10703**, 1266–1277, SPIE (2018).

[4] Ruane, G., Riggs, A., Mazoyer, J., Por, E. H., N'Diaye, M., Huby, E., Baudoz, P., Galicher, R., Douglas, E. and Knight, J., "Review of high-contrast imaging systems for current and future ground-and space-based telescopes I: coronagraph design methods and optical performance metrics," Space Telescopes and Instrumentation 2018: Optical, Infrared, and Millimeter Wave **10698**, 851–869, SPIE (2018).

[5] Goździewski, K., Niedzielski, A., Schneider, J. and Serabyn, E., "High-contrast Coronagraphic Techniques," European Astronomical Society Publications Series **42**, 79–90 (2010).

[6] Mawet, D., Riaud, P., Absil, O. and Surdej, J., "Annular groove phase mask coronagraph," The Astrophysical Journal **633**(2), 1191 (2005).

[7] Foo, G., Palacios, D. M. and Swartzlander, G. A., "Optical vortex coronagraph," Optics letters **30**(24), 3308–3310 (2005).

[8] Mawet, D., Serabyn, E., Liewer, K., Hanot, C., McEldowney, S., Shemo, D. and O'Brien, N., "Optical vectorial vortex coronagraphs using liquid crystal polymers: theory, manufacturing and laboratory demonstration," Optics Express **17**(3), 1902–1918 (2009).

[9] Rozas, D., Law, C. T. and Swartzlander, G. A., "Propagation dynamics of optical vortices," JOSA B **14**(11), 3054–3065 (1997).

[10] Swartzlander, G. A., Ford, E. L., Abdul-Malik, R. S., Close, L. M., Peters, M. A., Palacios, D. M. and Wilson, D. W., "Astronomical demonstration of an optical vortex coronagraph," Optics express **16**(14), 10200–10207 (2008).

[11] Berry, M. V., "The adiabatic phase and Pancharatnam's phase for polarized light," Journal of Modern Optics **34**(11), 1401–1407 (1987).

[12] Niv, A., Biener, G., Kleiner, V. and Hasman, E., "Manipulation of the Pancharatnam phase in vectorial vortices," Optics express **14**(10), 4208–4220 (2006).

[13] Delacroix, C., Absil, O., Forsberg, P., Mawet, D., Christiaens, V., Karlsson, M., Boccaletti, A., Baudoz, P., Kuittinen, M. and Vartiainen, I., "Laboratory demonstration of a mid-infrared AGPM vector vortex coronagraph," Astronomy & Astrophysics **553**, A98 (2013).

[14] Mawet, D., Absil, O., Delacroix, C., Girard, J. H., Milli, J., O'neal, J., Baudoz, P., Boccaletti, A., Bourget, P. and Christiaens, V., "L'-band AGPM vector vortex coronagraph's first light on VLT/NACO-Discovery of a late-type companion at two beamwidths from an F0V star," Astronomy & Astrophysics **552**, L13 (2013).

[15] Delacroix, C., Absil, O., Mawet, D., Hanot, C., Karlsson, M., Forsberg, P., Pantin, E., Surdej, J. and Habraken, S., "A diamond AGPM coronagraph for VISIR," Ground-based and Airborne Instrumentation for Astronomy IV **8446**, 1169–1177, SPIE (2012).

[16] Defrere, D., Absil, O., Hinz, P., Kuhn, J., Mawet, D., Mennesson, B., Skemer, A., Wallace, K., Bailey, V. and Downey, E., "L'-band AGPM vector vortex coronagraph's first light on LBTI/LMIRCam," Adaptive Optics Systems IV **9148**, 1330–1338, SPIE (2014).

[17] Castellá, B. F., Serabyn, E., Mawet, D., Absil, O., Wizinowich, P., Matthews, K., Huby, E., Bottom, M., Campbell, R. and Chan, D., "Commissioning and first light results of an L'-band vortex coronagraph with the Keck II adaptive optics NIRC2 science instrument," Adaptive Optics Systems V **9909**, 697–710, SPIE (2016).

[18] Absil, O., Mawet, D., Karlsson, M., Carlomagno, B., Christiaens, V., Defrère, D., Delacroix, C., Castella, B. F., Forsberg, P. and Girard, J., "Three years of harvest with the vector vortex coronagraph in the thermal infrared," Ground-based and Airborne Instrumentation for Astronomy VI **9908**, 99080Q, International Society for Optics and Photonics (2016).

[19] Catalán, E. V., Huby, E., Forsberg, P., Jolivet, A., Baudoz, P., Carlomagno, B., Delacroix, C., Habraken, S., Mawet, D. and Surdej, J., "Optimizing the subwavelength grating of L-band annular groove phase masks for high coronagraphic performance," Astronomy & Astrophysics **595**, A127 (2016).

[20] Maire, A.-L. K., Huby, E., Absil, O., Zins, G., Kasper, M., Delacroix, C., Leveratto, S., Karlsson, M., Ruane, G. J. and Käufl, H.-U., "Design, pointing control, and on-sky performance of the mid-infrared vortex coronagraph for the VLT/NEAR experiment," Journal of Astronomical Telescopes, Instruments, and Systems **6**(3), 035003 (2020).
[21] Brandl, B., Bettonvil, F., van Boekel, R., Glauser, A., Quanz, S., Absil, O., Amorim, A., Feldt, M., Glasse, A., Güdel, M., Ho, P., Labadie, L., Meyer, M., Pantin, E., van Winckel, H., and METIS Consortium., "METIS: The Mid-infrared ELT Imager and Spectrograph," The Messenger **182**, 22–26 (2021).
[22] Brandl, B. R., Absil, O., Agócs, T., Baccichet, N., Bertram, T., Bettonvil, F., van Boekel, R., Burtscher, L., van Dishoeck, E. and Feldt, M., "Status of the mid-IR ELT imager and spectrograph (METIS)," Ground-based and Airborne Instrumentation for Astronomy VII **10702**, 107021U, International Society for Optics and Photonics (2018).
[23] Agócs, T., Zuccon, S., Jellema, W., van den Born, J., ter Horst, R., Bizenberger, P., Vazquez, M. C. C., Todd, S., Baccichet, N. and Straubmeier, C., "End to end optical design and wavefront error simulation of METIS," Ground-based and Airborne Instrumentation for Astronomy VII **10702**, 107029O, International Society for Optics and Photonics (2018).
[24] Carlomagno, B., Delacroix, C., Absil, O., Cantalloube, F., de Xivry, G. O., Pathak, P., Agocs, T., Bertram, T., Brandl, B. R. and Burtscher, L., "METIS high-contrast imaging: design and expected performance," Journal of Astronomical Telescopes, Instruments, and Systems **6**(3), 035005 (2020).
[25] Kenworthy, M. A., Absil, O., Carlomagno, B., Agócs, T., Por, E. H., Bos, S., Brandl, B. and Snik, F., "A review of high contrast imaging modes for METIS," Ground-based and Airborne Instrumentation for Astronomy VII **10702**, 10702A3, International Society for Optics and Photonics (2018).
[26] van Boekel, R., "In- and out-of-pupil thermal background estimates," METIS internal document E-REP-MPIA-MET-1100, version 1.3 (2021).
[27] Delacroix, C., Absil, O., Orban de Xivry, G., Shinde, M., Pathak, P., Cantalloube, F., Carlomagno, B., Christiaens, V., Boné, A., Dolkens, D., Kenworthy, M. A. and Doelman, D., "The High-contrast End-to-End Performance Simulator (HEEPS): influence of ELT/METIS instrumental effects," Modeling, Systems Engineering, and Project Management for Astronomy X, SPIE (2022).
[28] Käufl, H.-U., Kasper, M., Arsenault, R., Jakob, G., Leveratto, S., Zins, G., Fuenteseca, E., Riquelme, M., Siebenmorgen, R. and Sterzik, M., "NEAR: new earths in the Alpha Cen Region (bringing VISIR as a" visiting instrument" to ESO-VLT-UT4)," Ground-based and Airborne Instrumentation for Astronomy VII **10702**, 107020D, International Society for Optics and Photonics (2018).